UNIVERSITY OF CALIFORNIA,
IRVINE

Single-Molecule Measurements of T4 Lysozyme using Carbon Nanotube Electronic Circuits

THESIS

submitted in partial satisfaction of the requirements
for the degree of

MASTER OF SCIENCE

in Physics

by

Patrick Craig Sims

Thesis Committee:
Professor Philip G. Collins, Chair
Professor Gregory A. Weiss
Professor Zuzanna S. Siwy

2014

DEDICATION

To

my family,

for the unconditional love, constant care, and unwavering support;

my friends,

for the camaraderie and adventures that we share;

and my azizam, Lili,

for being the sparkling gem that illuminates my life.

TABLE OF CONTENTS

Page

LIST OF FIGURES

Page

LIST OF TABLES

Page

ACKNOWLEDGMENTS

I would like to show my utmost appreciation for Professor Philip G. Collins for providing an outstanding scientific environment to conduct this research. His guidance and insight played a critical role in the realization of this work and in furthering my understanding of nanoelectronic systems.

Furthermore, I would like to thank Professor Gregory A. Weiss for collaborating, advising, and assisting with the biological and chemical aspects of this work. Without his helping hand, this work would have proved to be insurmountable.

Undoubtedly, none of this would have been possible without my friends and colleagues in both the Collins and Weiss laboratories. I would like to express my thanks to Steve Hunt, Danny Wan, Israel Perez, Tatyana Sheps, Brad Corso, Issa Moody, Tivoli Olsen, Chengjun Dong, Deng Pan, Elliot Fuller, Tolga Gul, Max Akhterov, Mariam Iftikhar, and of course, Doctor Yongki Choi, who mentored me throughout this work.

ABSTRACT OF THE THESIS

Single-Molecule Measurements of T4 Lysozyme using Carbon Nanotube Electronic Circuits

By

Patrick Craig Sims

Master of Science in Physics

University of California, Irvine, 2014

Professor Philip G. Collins, Chair

Because of their unique electronic and chemical properties, single-walled carbon nanotubes (SWNTs) are attractive candidates for label-free, single-molecule sensing and detection applications. In this work, a field-effect transistor (FET) architecture comprised of an individual SWNT is used to transduce the conformational motion of a single T4 lysozyme protein, conjugated to the SWNT side wall, into a corresponding electrical current signal. The SWNTs are grown using chemical vapor deposition, and metal electrical contacts are formed using electron beam evaporation. Using N-(1-Pyrene)maleimide, the protein is conjugated to the SWNT side wall. After conjugation, the sensing area of the device is submerged in an electrolyte solution, and the source-drain current is measured while applying an electrolyte-gate. Analysis of the signal provided single-molecule resolution of the dynamical activity of lysozyme as it hydrolyzes macromolecular peptidoglycan, a component of bacterial cell walls. This analysis revealed seven different independent time scales that govern the activity of lysozyme, the pH dependence of these time scales, and a lower limit on the number rate-limiting steps in

lysozyme's hinge opening and closing motions. Furthermore, the signals elucidated differences in how lysozyme traverses and catalyzes structurally varying peptidoglycan constructs.

Chapter 1

Introduction

Single-walled carbon nanotubes (SWNTs) are cylindrical nanostructures consisting of a rolled-up monolayer of a hexagonal network of sp2 hybridized carbon, or graphene. These sheets of graphene can be rolled-up at quantized angles, i.e., chiral angles, forming quasi-one-dimensional cylinders. Because of their lattice structure, SWNTs exhibit exquisite electronic properties that depend directly on the chiral angle; the chiral angle dictates whether a pristine SWNT is metallic or semiconducting. Their coveted electronic as well as thermal properties have directed the exploration of using SWNTs as next generation field-effect transistors (FETs) and interconnects for very-large-scale-intergration (VLSI) in the semiconducting industry, but the challenges involved in the fabrication process, such as controlling the alignment, purity, contact resistance, and type of SWNTs, have prevented the widespread implementation of this material in these technologies.

While SWNT FETs may be ill-suited for implementation into digital electronics, they have superior properties for use in sensing applications: quasi-ballistic electron transport, comprised of entirely surface exposed atoms, carbon-based, and chemically inert under most conditions. Because of their quasi-ballistic nature, scattering within the SWNT with itself, i.e., electron-electron or electron-phonon scattering, is minimal, and, thereby, makes the conduction through a SWNT FET sensitive to additional scattering sites either due to physisorption, chemisorption, or

charges in the local environment near the SWNT. Since SWNTs are comprised entirely of surface-exposed atoms, their conduction electrons intimately interact with the encompassing environment imparting the SWNT with sensitivity of its surroundings. Ultimately, the sensitivity of SWNT FETs[1-3] originates from their quasi one-dimensional electronic structure and low carrier concentration. Heller et al. clearly summarized the various possible mechanisms that can contribute to chemical sensing by SWNT FETs and tried to distinguish among them[4]. In certain cases, charge transfer doping or chemisorption events were shown to be the main cause of slow, chemiresistive responses. Others have proven that interfacial effects at SWNT-electrode junctions can play important roles[5,6]. Beyond sensitivity, a good sensor requires selectivity. Due to the versatility of carbon, well-characterized organic chemistry techniques and protocols provide chemical means to attach functional groups or large molecules such as DNA or proteins to the sidewall of the SWNT, endowing the SWNT with selective sensitivity. Due to the inertness of SWNTs resulting from sp2 hybridization, researchers have developed methods involving diazonium chemistry[7], electrochemical oxidation[8,9], and UV/Ozone oxidation[10], in order to introduce chemically reactive sites to covalently bind specific molecules to the SWNT sidewall. Other approaches have used non-convalent interactions such as π-π stacking[11] that use a molecule comprised of an anchor, aromatic carbon rings that adhere to the nanotube sidewall, and a tail, a reactive functional group that is chemically modified to impart selectivity. Because of their sensitivity and selectivity, SWNT FETs provide a versatile platform for sensing applications.

Myriad single-molecule experimental techniques examine the dynamics and kinetics of single-molecules to uncover answers impossible to extract from conventional bulk ensemble

measurements[12]. These include ergodicity, transient motions, and short-lived intermediates. Common techniques to examine single-molecules, particularly enzymes, rely on fluorescence to report chemical reactions or molecular motions, and can yield both temporal and spatial information[13,14]. Nevertheless, the properties of fluorophores impose limitations on the duration and resolution of measurements due to photobleaching, intermittency, and limited photon counts. Because of the relationship between the exciting light source intensity, photon count, and photobleaching, any increase in the resolution is offset by a decrease in duration and vice versa. The necessity of fluorescent labels prevents the coupling of long-duration and high-resolution optical measurements for a single enzyme leaving a considerable gap in how individual enzymes contribute to biological processes and how their motions correlate to their catalytic function. Being label-free with high bandwidth capabilities, low-dimensional FET-based sensors offer an electronic approach to begin to fill in this void.

In general, electronic transduction using low-dimensional FET architectures is not unique to SWNTs[15-18] and has been explored using silicon nanowires[19-22], nanoclusters[23,24], graphene[25], and single molecules[26]. In most cases, slow changes in DC conductance have been suggestive of single-molecule detection, but the absence of dynamic responses undermined the general premise of high bandwidth detection. Recently, high-bandwidth dynamic transduction has been achieved in two single-molecule electronic architectures. In the first, DNA molecules threading through solid state pores have generated high-fidelity electronic signals that offer opportunities for DNA sequencing[27]. In the other approach, a more traditional FET architecture has leveraged amplification at SWNT point defects[9] to

demonstrate kinetic binding and unbinding, both for molecules interacting directly with the defect site[8] and indirectly through an attached biomolecule[28,29].

While the point defect approach provides single molecule sensitivity, it also suffers from significant limitations that prevent its widespread implementation due to the electrochemical introduction of a defect site into the SWNT sidewall. The device yield is considerably low as many devices open-circuit. Those that continue to conduct acquire additional noise and resistance which limits the ability to discern the desired signal. Furthermore, the defect site provides additional oxidative pathways that cause the SWNT devices to degrade and open-circuit over time.

Because of these impediments, we developed a non-covalent scheme, to be described in the chapters ahead, that circumvents these issues while retaining single molecule sensitivity. We then used the scheme to understand the dynamic behavior of T4 lysozyme and its processivity during catalysis.

Chapter 2

Experimental Design and Fabrication

2.1 Fabrication of Carbon Nanotube Field Effect Transistors

We fabricated SWNT FET devices on the wafer-scale using 4 inch degenerately doped (p++) silicon wafers with a 500 nm thermally formed insulating oxide layer. The constituent components for a FET are a semiconducting channel, a source electrode, a drain electrode, and a gate electrode. The device fabrication procedure consists of SWNT synthesis to form the transistor channel and clean room processing to lithographically define metal source and drain electrodes. Finally, the doped silicon and oxide layer define the electrostatic gate for the three-terminal device.

2.1.1 Carbon Nanotube Synthesis

To form SWNTs on these wafers, we used chemical vapor deposition (CVD). Growth of SWNTs deposition requires the use of a catalyst and a carbon feedstock, such as methane or ethanol, to promote the chemical formation of SWNTs. We synthesized a Keggin $Fe_{30}Mo_{84}$ catalyst nanoparticles using methods described previously[30,31]. These particles have been shown to produce SWNTs under suitable CVD conditions[32]. We spin-coated at 150 rpm a 10^3 dilution of a saturated catalyst solution dissolved in ethanol to distribute the nanoparticles dilutely and arbitrarily on the surface of the wafer. Next, the wafer undergoes a thermal

oxidation in air at 700°C to oxidize and decompose organic ligands of the catalyst particles. The wafer is inserted into a 6 inch quartz-tube furnace at 940°C. The furnace is then purged with Argon gas (3000 sccm) to achieve reproducible and chemically inert initial reaction conditions. To activate the catalyst, we use a gas mixture (940°C, 520 sccm H_2 in 3000 sccm Ar) to reduce the oxidized nanoparticles. Next, we expose the activated catalyst to a carbon feedstock gas mixture (940°C, 1000 sccm CH_4 and 520 sccm H_2 in 3000 sccm Ar) for 5 minutes to promote the SWNT formation reaction. To quench the reaction and to limit SWNT oxidation, we purge again using Ar gas and position the wafer in a region where the temperature is less than 400°C to minimize combustion reactions. This recipe reproducibly yields SWNTs with diameters of 1.1-1.6 nm and areal densities of 0.01 SWNTs/μm^2. A scanning electron microscope (SEM, Philips XL-30 at 1 kV) is used to determine the areal density and an atomic force microscope(AFM, Pacific Nanotechnology Nano-R and NT-MDT) is used to measure the SWNT diameter.

2.1.2 Clean Room Processing

Upon completion of the CVD procedure, we transfer the wafers to the clean room to form the source and drain metal electrodes. Using optical lithography and electron-beam evaporation, metal interdigitated electrodes with separations of 2 – 3 μm are formed on top of the arbitrarily-grown SWNTs.

With the SWNT devices fabricated, each device is electronically characterized to determine resistance, transconductance, and type, i.e., semiconducting or metallic. Candidate devices are then characterized using atomic force microscopy to ensure that only a single SWNT spans the

source-drain electrodes, to measure the SWNT diameter, and to confirm that it is free from any particulates.

To mitigate any Schottky barrier effects due to work function changes at the metal/nanotube interface and to minimize leakage current, the entire device is passivated in electron beam resist (A3 PMMA, MicroChem). Electron beam lithography was then used to define a channel that exposed a 0.5 – 1.0 μm wide active region of the SWNT sidewall while protecting the source and drain electrodes. The exposed active region width was chosen to increase the likelihood of successfully conjugating a protein to the sidewall of the SWNT and to decrease the possibility of accidentally exposing the source and drain electrodes when patterning the active region.

2.2 Protein Conjugation

To conjugate the protein to the SWNT, we used a bifunctional linker molecule, N-(1-Pyrene)maleimide, to tether a protein to the SWNT side. Pyrene non-covalently adsorbs to the sidewall of the nanotube via π- π interaction[11], and the maleimide group of the molecule forms stable thioether bonds[33] with a thiol of a cysteine sidechain of a protein. As a necessary condition, the conjugation mechanism requires that the protein to be studied contains at least one surface exposed cysteine. Imposing a stricter condition that the protein contains only one cysteine restricts the attachment reaction to proceed at a single site on the protein.

The conjugation protocol follows here. The devices were soaked in a saturated solution of N - (1 - Pyrene)maleimide (Sigma Aldrich) dissolved in ethanol for 30 min. Next, the devices were

either soaked for up to 30 min in 0.1% Tween-20 (Acros Organics) in ethanol or were rinsed with 3 – 5 mL of the solution. Both methods yielded single protein functionalized devices. The devices were then rinsed under flowing de-ionized water from 1 – 5 min. The devices were submerged in a 50 μM solution of T4 Lysozyme in PBS (140 mM NaCl, 2.7 mM KCl, 8.1 mM Na_2HPO_4, 1.5 mM KH_2PO_4, pH 7.2) for 60 min without agitation. The devices were soaked in wash buffer (5 mM KCl, 10 mM Na_2HPO_4, 0.05% Tween-20, pH 7) for 30 min with agitation to remove unattached lysozyme from the device surface. Upon completion, the devices were rinsed under flowing de-ionized water from 1 – 5 min and submerged in PBS until measured.

Protein conjugation was confirmed either before or after electrical measurements. To confirm conjugation before conducting electrical measurements, the devices were imaged in PBS using liquid atomic force microscopy (NT-MDT). To confirm conjugation after measurements, the devices were rinsed for 1 – 2 min in deionized water, dried, and imaged. Figure 2.1 (A) is an example device before the electron beam resist, with a dashed line indicating the desired position of the window. Figure 2.1 (B) shows the same device after electron beam lithography and protein conjugation, now with two lysozyme proteins attached. Figure 2.1 (C) shows another device in which only one attachment occurred. AFM line cuts are provided in Figure 2.1 (D) for the six devices. In each line cut, the pyrene-coated SWNTs appear to be 1.5 – 2.0 nm in height, while the attachment sites are 5 – 10 nm high. The difference is much more than the surface roughness along the rest of the SWNT, which we measure to be 0.2 – 0.4 nm. The range of heights observed at the lysozyme attachment site is consistent with the molecule's physical structure, especially considering that it can attach in different orientations around the SWNT circumference and that these particular images were acquired after drying the device.

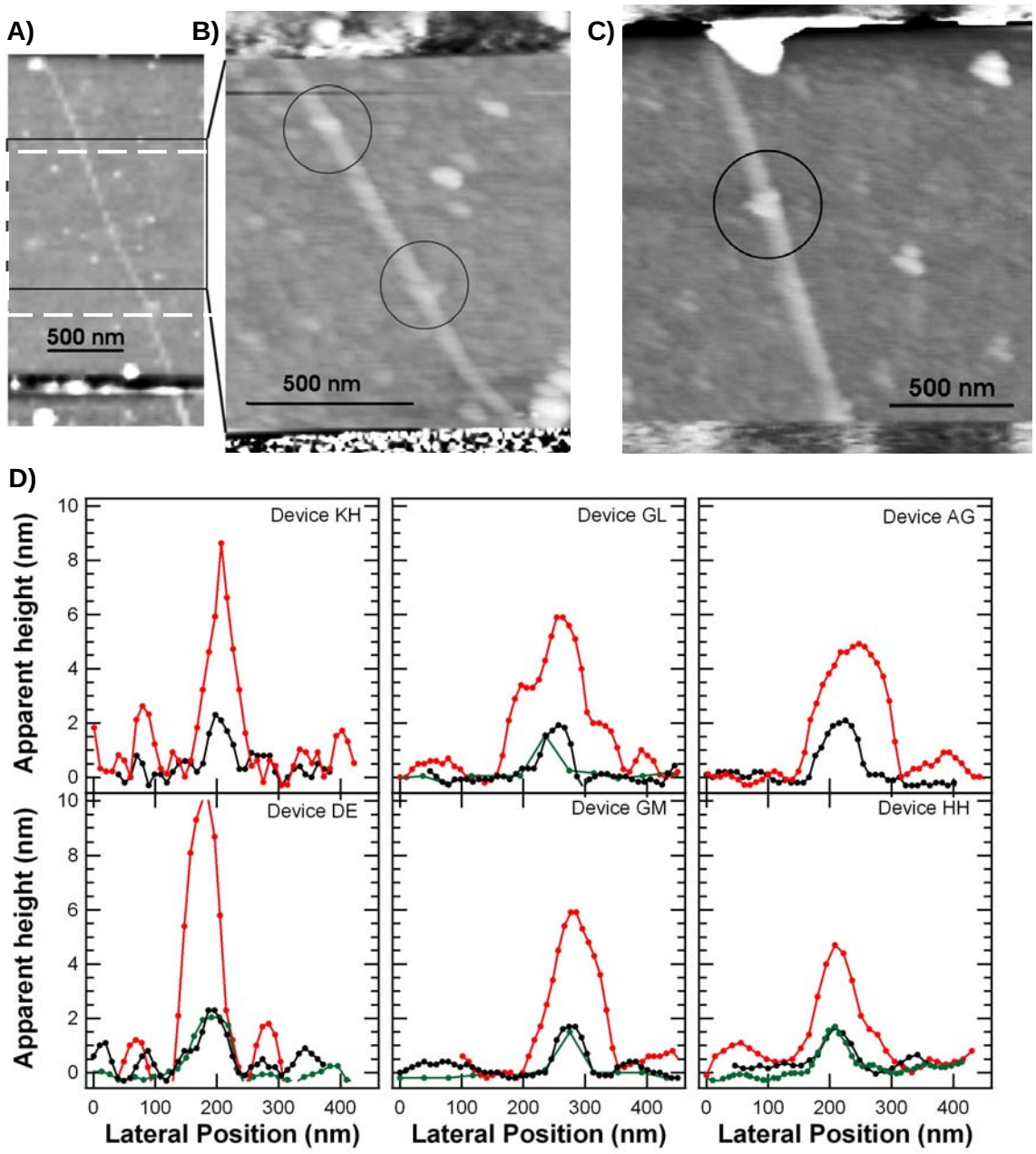

Figure 2.1: Examples of lysozyme device fabrication. (A) AFM image of a bare SWNT device with the target position of the PMMA window indicated (dashed box). (B) A higher magnification image of the same device after bioconjugation, which resulted in two lysozyme attachments (gray circles). Note the larger scale bar, and that the top and bottom edges of the image now correspond to the protective PMMA rather than to metal electrodes. (C) A device with a single lysozyme attachment. (D) AFM line profiles for 6 different devices. Three lines in each image correspond to height profiles taken across the lysozyme attachment (red), pyrene-coated SWNT (black), and pristine SWNT (green). Reproduced from [34].

Protein solutions of T4 lysozyme variants were prepared in the laboratory of Professor Gregory Weiss by former graduate student, Dr. Issa S. Moody; and graduate student, Tivoli J. Olsen. The variants of T4 lysozyme were created using site-directed mutagenesis. Circular dichroism was used to ensure proper protein folding, and bulk assays were used to determine relative catalytic activity. The methods can found in previous reports[34-36]. The following is a list of each T4 lysozyme variant measured:

1. **S90C:** an active variant of pseudo-wild-type T4 Lysozyme where cysteine replaces a serine at the 90-site and the naturally-occurring cysteines have been replaced with a threonine at the 54-site and an alanine at the 97-site.
2. **S36C:** an active variant of pseudo-wild-type T4 Lysozyme where cysteine replaces a serine at the 36-site and the naturally-occurring cysteines have been replaced with a threonine at the 54-site and an alanine at the 97-site.
3. **R119A:** an active variant of S90C where an arginine near the 90-site is replaced with an alanine.
4. **K83A:** an active variant of S90C where a lysine near the 90-site is replaced with an alanine.
5. **K83A/R119A:** an active variant of S90C where a lysine and arginine near the 90-site are both replaced with alanines.
6. **K83E/R119A:** an active variant of S90C where a lysine and arginine near the 90-site are replaced by glutamic acid and alanine, respectively.

7. **K83A/R119E:** an active variant of S90C where a lysine and arginine near the 90-site are replaced by alanine and glutamic acid, respectively.
8. **K83E/R119E:** an active variant of S90C where a lysine and arginine near the 90-site are both replaced by glutamic acids, respectively.
9. **T26E:** an inactive variant of S90C where a threosine at the 26-site is replaced by a glutamic acid. This variant produces a covalent adduct with the peptidoglycan substrate and thus provides a constitutively substrate-bound version of the lysozyme[37].
10. **E11H:** an inactive variant of S90C where a glutamic acid is replaced by a histidine[37].

2.3 Electrical Measurements

Electrical measurements were performed on the protein conjugated SWNT FET. A source-drain bias (V_{sd}) of 100 mV was applied using an NI-DAQ output. Using an optical microscope and micromanipulators, a droplet of electrolytic solution positioned over the active region of device served as the gate. The potential of the electrolytic solution was controlled using Pt counter and pseudo-reference electrodes, and was held at a fixed potential in the range of -0.2 – 0.2 V versus Pt (V_{RE}) using a Keithley 2400 sourcemeter. The source-drain current (I_{sd}) was measured using a current-to-voltage converter (Keithley 428 preamplifier) operating at 10^7 or 10^8 V/A gain with rise times of 15 and 40 μs, respectively. The NI-DAQ measured the current-to-voltage converter output at a sampling rate of 100 kHz. $I_{sd}(t)$ for each measurement condition was collected for a minimum of 600 s.

Chapter 3

Single-Molecule Electronic Measurements of T4 Lysozyme

3.1 Introduction

This chapter demonstrates that single-molecule dynamics can be monitored by attaching a single protein molecule of interest to a field-effect transistor (FET) device (Figure 3.1 (A)). Signal amplification was achieved by allowing the charged functionalities on the surface of the protein to electrostatically gate the underlying FET. By exploiting the low dimensionality and extreme local gate sensitivity of single-walled carbon nanotube (SWNT) FETs, molecular motions create changes in electrostatic potentials that can be converted into dynamically changing electron fluxes. Such signals are similar to the photon fluxes in fluorescence experiments, but with advantageous bandwidth and shot noise limitations.

We accomplished single-molecule transduction very similar to the work of Sorgenfrei *et al.* [28,29], but using a non-covalent bioconjugation strategy that provides a high device-fabrication yield. Rather than introducing a defect, tailoring its chemistry, and then conjugating that site to the target molecule, our method used non-covalent immobilization based on pyrene linkers[11], as described in the experimental methods chapter.

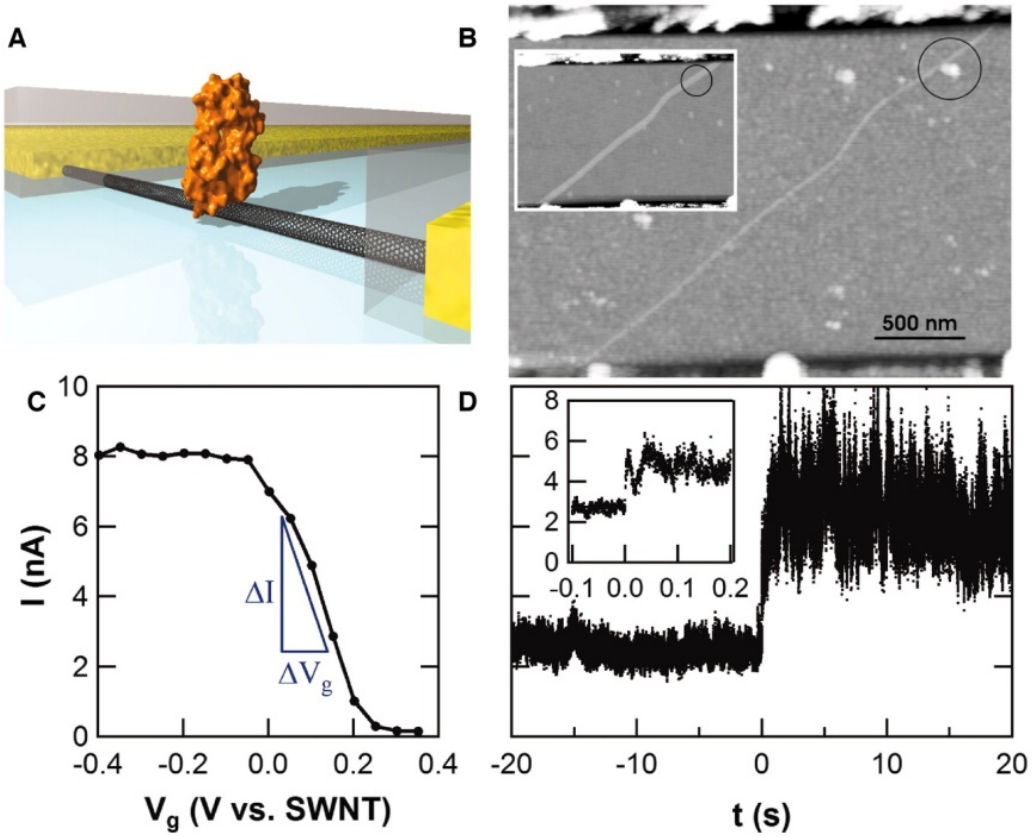

Figure 3.1: (A) Schematic diagram of the single lysozyme being interrogated by a carbon nanocircuit. The partial poly(methyl methacrylate) coating is depicted in gray. (B) AFM topography of a SWNT FET before (inset) and after coating with the pyrene linker, lysozyme incubation, and washing to reduce nonspecific binding. The circle highlights the point of lysozyme attachment. (C) Response of current in a lysozyme device to electrolytic gating. (D) I(t) measured in phosphate buffer, with peptidoglycan substrate (25 μg/mL) added to the solution at t = 0. The inset with a magnified time axis indicates a rapid response of <50 ms (inset). Reproduced from [34].

Atomic force microscopy (AFM) before functionalization and after completion of the measurements (Figure 3.1 (B)) confirmed the presence of a single attached lysozyme. Lysozyme is ~7 nm in size, which made it easily distinguishable when attached to a 1- to 2-nm-diameter SWNT. In addition to microscopy, electrical characterization was performed at each fabrication stage. Figure 3.1 (C) shows the gate dependence of the source-drain current $I(V_G)$ in a completed lysozyme device, measured with aqueous electrolyte (phosphate-buffered saline) in

direct contact with the SWNT sidewall[38]. In general, the coating technique added 1 to 2 megohms of series resistance to the SWNT conductor and shifts its $I(V_G)$ curve, in accord with previous reports[15,39,40]. Finally, Figure 3.1 (D) displays the typical device response $I(t; V_G = 0)$ upon introduction of the lysozyme substrate, peptidoglycan (Sigma-Aldrich). A polysaccharide found in bacterial cell walls, peptidoglycan consists of N-acetylmuramate (NAM)-N-acetylglucosamine (NAG) repeating units, and lysozyme catalyzes the hydrolysis of its glycosidic bonds[41]. Chemoresistive responses of this nature are widely reported for nanodevices, and SWNT conductance can be quite sensitive to slight environmental changes, even when they are not decorated with proteins[1,2,42].

The time-averaged, DC response depicted in Figure 3.1 (D) underlies the classification of such devices as chemical or biological "sensors." However, analysis of the dynamic response, not the DC level, can provide insights into conformational changes of the attached single protein. The magnitude of I(t) fluctuations increased immediately when peptidoglycan substrate was added, and, after one or more seconds of equilibration, these fluctuations developed into a two-level, random telegraph signal (RTS) that can be statistically analyzed.

3.2 Background and Control Measurements

In every experiment, the presence or absence of RTS fluctuations was a reliable predictor of the simultaneous presence of the peptidoglycan substrate and a SWNT-bound, catalytically functional variant of lysozyme.

3.2.1 Response of Bare SWNT to Test Analytes

Control measurements tested for any dynamic response of the SWNT sidewall to the PBS buffer, or to the substrate molecules used to probe the dynamics of lysozyme. As shown in Figure 3.2, unfunctionalized devices with PMMA windows showed no electronic signals that might be associated with dynamic interactions. No part of the noise power spectrum (DC – 10 kHz) was sensitive to the presence of substrate molecules. After this initial test, the same SWNT devices were rinsed clean and conjugated to lysozyme. With the added pyrene and lysozyme, devices that previously had no response showed two level fluctuations when probed with substrate.

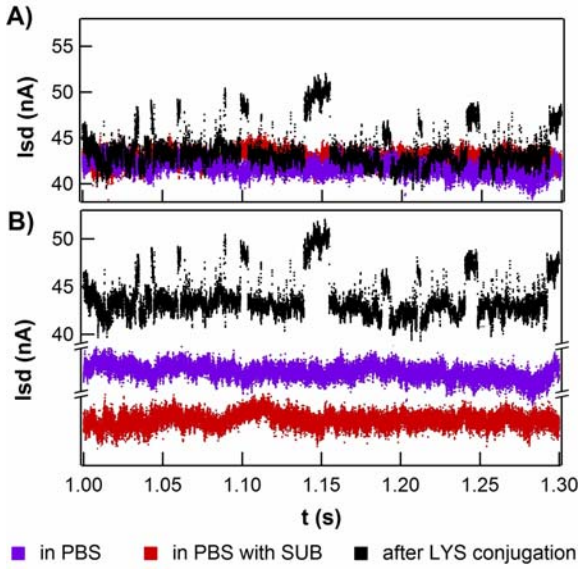

Figure 3.2: Bare SWNT control experiments. (A) Plot shows typical I(t) fluctuations for a bare SWNT measured in PBS buffer, without substrate (purple) or with substrate (red) present. Subsequently, the same device is functionalized with pyrene and lysozyme, and then remeasured in PBS with substrate (black data). (B) The same data, offset from the functional device for clarity. Reproduced from [34].

3.2.2 Response of Pyrene-coated SWNT to Test Analytes.

Additional control measurements tested for any dynamic response of the pyrene-coated SWNT sidewall. This control is particularly relevant because the final devices consist of a relatively high number of pyrene molecules coating the entire SWNT, whereas the lysozyme attachments are very dilute. In the absence of lysozyme, pyrene-coated SWNTs were measured in PBS, and in the same PBS solutions of substrate molecules used to probe the dynamics of lysozyme. As shown in Figure 3.3, pyrene-coated SWNTs showed no dynamic electronic response to the reagents. The same devices, after performing the lysozyme coupling reaction, exhibited two level fluctuations with substrate present. One notable part of Figures 3.2 and 3.3 is a small change in the DC current level. In general, the pyrene coating step tends to increase device conductance by 1-2 megohms, whereas subsequent protein conjugation decreases the conductance. A cancellation is observed in Figure 3.2, where a bare m-SWNT device has nearly the same current level after the combination of pyrene coating and protein conjugation. On the other hand, Figure 3.3 compares a pyrene-coated device before and after protein conjugation, in which case an offset is clearly observed. Note that Figures 3.2 and 3.3 are collected from different devices that by coincidence have similar resistances of 2.0 – 2.5 megohms.

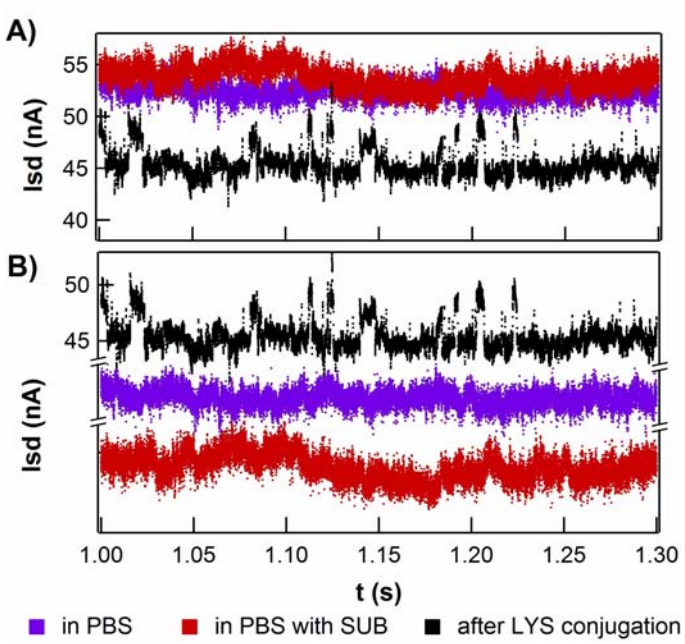

Figure 3.3: Pyrene-coated SWNT control experiments. (A) Plot shows typical $I(t)$ fluctuations for a pyrene-coated SWNT measured in PBS buffer, without substrate (purple) or with substrate (red) present. Subsequently, the lysozyme coupling reaction is performed on the same device, and then it is remeasured in PBS with substrate (black data). Note that the lysozyme coupling reaction decreases the device conductance by approximately 10%. (B) The same data, offset from the functional device for clarity. Reproduced from [34].

3.2.3 Electrical Noise of Bioconjugated SWNT Devices

The noise characteristics of SWNT devices are typically unchanged by bioconjugation (Figure 3.4). Direct comparison of the spread of fluctuations $\Delta I(t)$ around a time-averaged mean cannot distinguish the addition of protein to a device when measured in PBS. The similarity in Figure 3.4 (C) indicates that lysozyme's native variability and thermal fluctuations do not induce noise above the baseline electrical noise generated by the SWNT itself. Small changes in the DC conductance do occur, and the precise spectral content of the noise can vary from one device to another; however, these changes do not affect the current distribution.

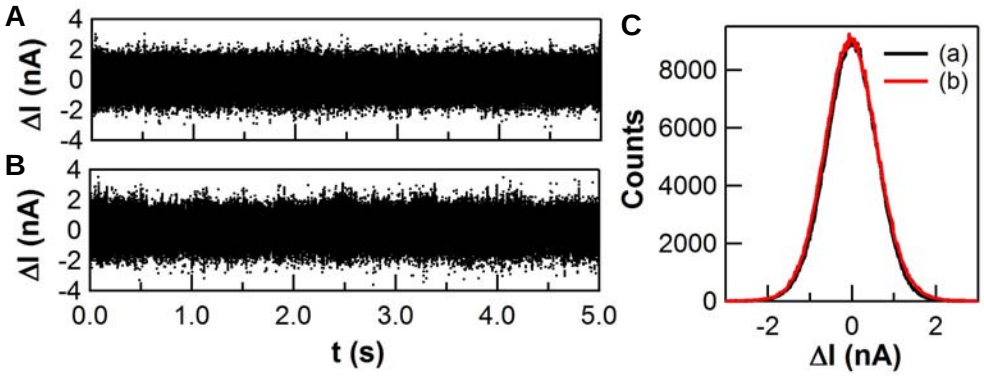

Figure 3.4: I(t) signals from a typical SWNT device (A) before and (B) after lysozyme bioconjugation. (C) Histograms of the two signal distributions are indistinguishable. Reproduced from [36].

3.2.4 Response of Devices with Inactive Lysozyme Variants.

The control experiments above provide compelling evidence that the two level fluctuations are specific to lysozyme-substrate interactions. Fluctuations are not caused by the SWNT device, by the pyrene coating, by the PBS buffer or substrate, or by the lysozyme itself in the absence of substrate.

To further test the source of the observed two-level fluctuations, we fabricated SWNT devices with the catalytically inactive variants of lysozyme T26E and E11H[37]. The two mutated residues, Thr26 and Glu11, play key roles in the lysozyme mechanism for the catalysis of glycoside hydrolysis. The T26E variant produces a covalent adduct with the peptidoglycan substrate, and thus provides a constitutively substrate-bound version of the lysozyme. The E11H variant is also catalytically inoperable, but does not form a covalent bond to the substrate.

Twelve devices were fabricated using the same methods described above, but using the T26E (eight devices) or E11H (four devices) variants. Upon the addition of substrate, all twelve devices prepared with an inactive lysozyme variant were equally quiet with and without substrate present, and no two level fluctuations were observed. Two examples of this are shown in Figure 3.5. The absence of two level fluctuations in all 12 devices is markedly different from the 80% success rate we observe in devices that contain the active, S90C variant. AFM imaging of the devices indicated successful, single protein attachments with both T26E and E11H, and two example images are shown in Figure 3.5 (D). The point mutations had no apparent effect on the attachment yield and the topographical AFM images were indistinguishable among the different variants.

The successful attachment and the absence of fluctuations together confirm that the observed signals are specific to the catalytic processing of lysozyme. This series of control experiments rules out the possibility that noncatalytic, merely electrostatic interactions between lysozyme and substrate might be causing the two level fluctuations.

As an aside, we note that the two inactive variants E11H and T26E are not easily distinguishable by our SWNT device technique, despite the fact that T26E permanently binds substrate and E11H does not. Our measurements suggest that an initial binding event by the T26E may cause a single, step-like increase in I(t), but in general such isolated events are difficult to distinguish from the low frequency, $1/f$ fluctuations of the SWNT itself. All of the analysis described here is

completed with the aid of a 10 Hz highpass filter to minimize this SWNT noise, and that filtering eliminates the only evidence of a difference between the E11H and the T26E variants.

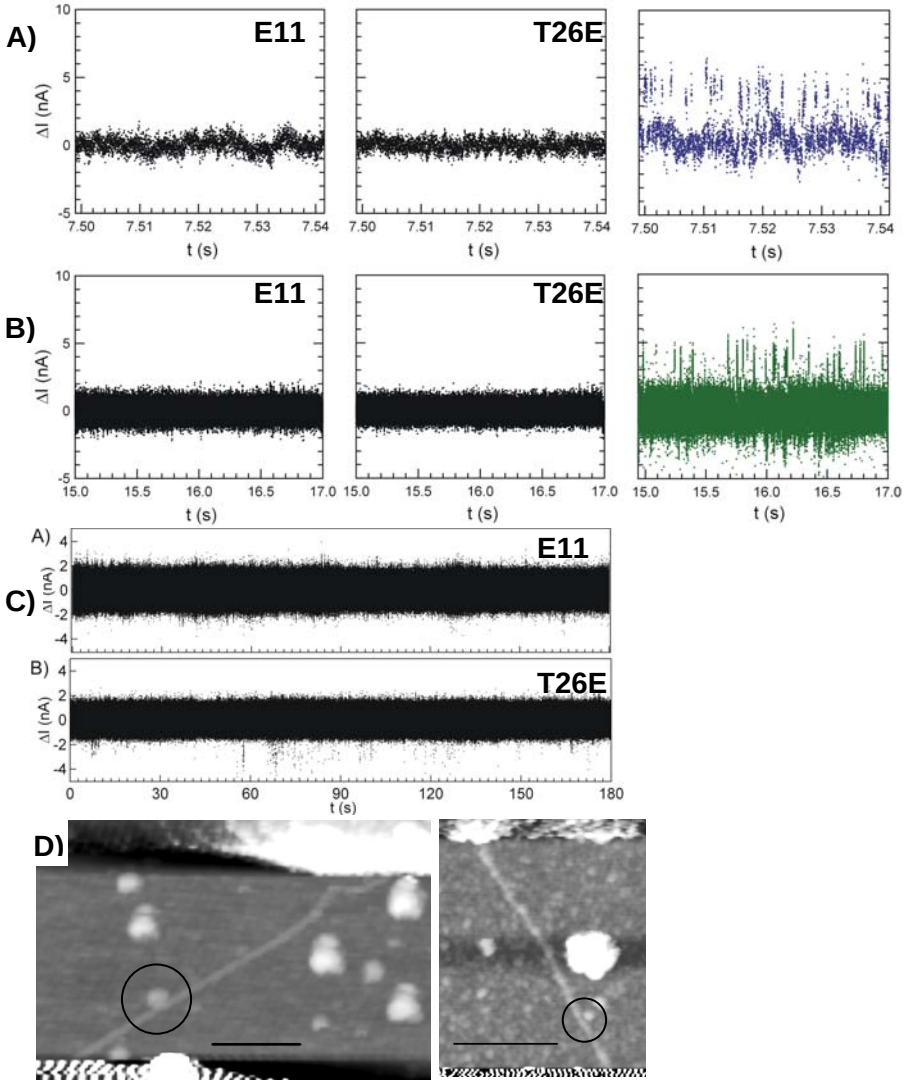

Figure 3.5: Control experiments with catalytically inactive lysozyme variants. The E11H and T26E lysozyme variants show no two-level switching when inspected over (A) 40 ms, (B) 2 s, or (C) 180 s intervals. For a direct comparison, Figures 3.6 (C, D) with comparable time-scales are reproduced here to show data from the active lysozyme variant discussed in the text. The E11H variant cannot bind substrate in its active site, and the T26E variant forms a long-lived, covalent bond to substrate with no catalytic activity. Note that when no switching is present, the experimental variable ΔI does not distinguish whether the enzyme is in its open or closed conformation. (D) Example AFM images of 2 of the 12 devices fabricated with inactive variants. Scale bars are 500 nm. Reproduced from [34].

3.3 Random Telegraph Signal of Catalytically Active T4 Lysozyme

Figure 3.6 (A) shows 30 s of raw data collected from a single lysozyme device, along with the time-varying mean computed with a 10-Hz digital filter. The lowest-frequency fluctuations had a $1/f$ spectral dependence and were indistinguishable from the noise incurred by a pristine SWNT in solution. Removing this slowly changing component, as shown in Figure 3.6 (B), greatly simplified further analysis. The higher-frequency components were revealed to be a two-level RTS with a constant amplitude distribution but two distinct RTS fluctuation rates. During some time periods, the RTS oscillated with a "fast" mean frequency of 316 Hz (Figure 3.6 (C)). At other times, the RTS oscillated with a "slow" mean frequency of 15.4 Hz (Figure 3.6(D)). The data in Figure 3.6 (C) are colored to differentiate the two types of RTS response and to emphasize their typical durations. Both the fast and the slow RTS segments lasted many seconds, suggestive of a long-term, two-state "memory" that was independent of the RTS itself. Accurate determination of the mean duration of this memory effect $\langle \tau_{mem} \rangle$ required that measurements be conducted for at least 600 s.

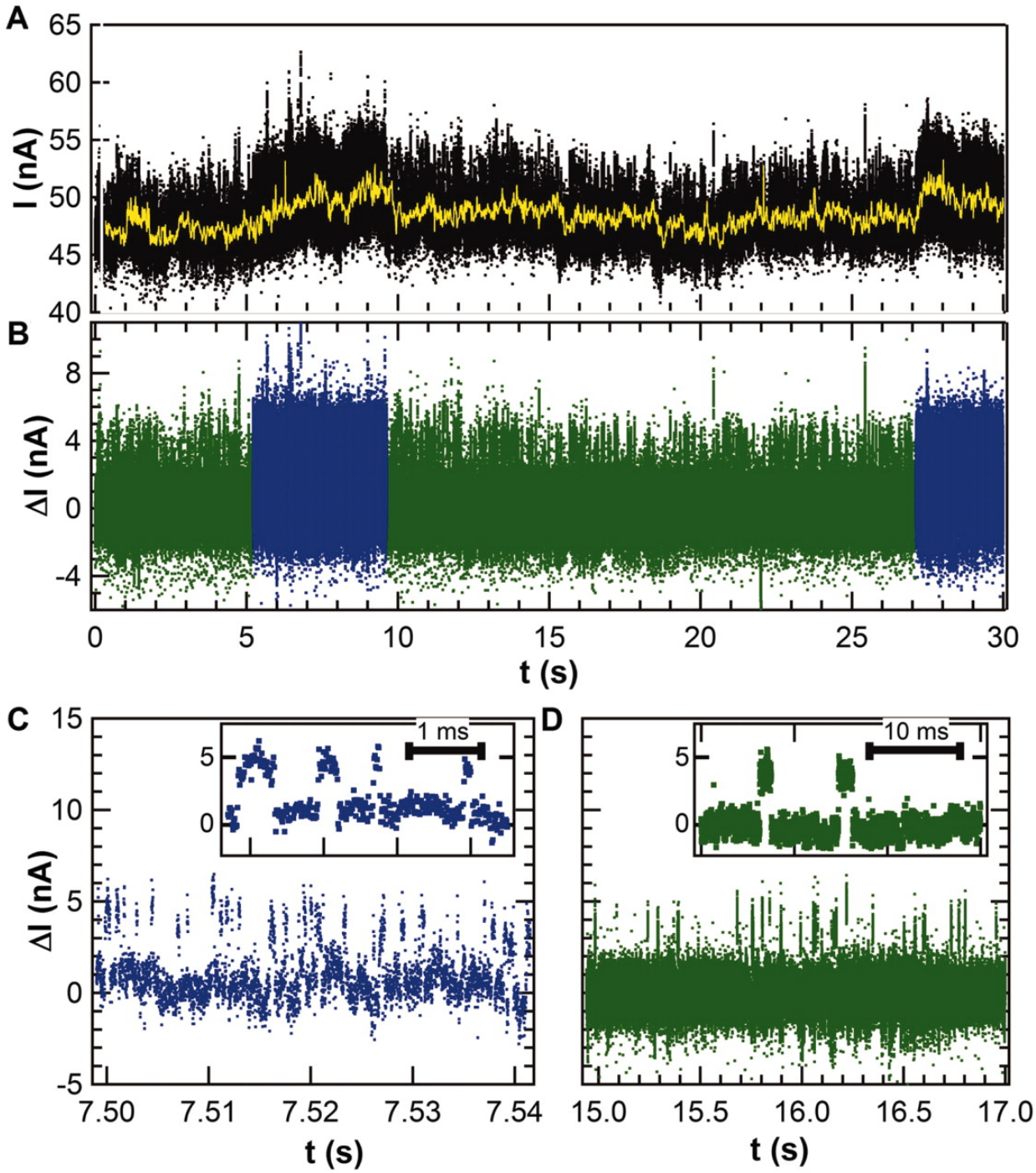

Figure 3.6: (A) Long-duration I(t) sequences exhibit dynamic noise on top of low-frequency fluctuations (yellow line) having a 1/*f* distribution. (B) Subtracting the meandering mean produces a filtered data set that clarifies the fluctuations as two-level, simplifies further analysis, and reveals that the two-level switching rates vary over 5- to 15-s periods. (C) The faster RTS oscillates about 300 times per second, whereas (D) the slower RTS oscillates 15 times per second. The insets show individual switching events for each case. Reproduced from [34].

3.3.1 Probability Distribution of RTS Events

The sequences of fast and slow RTS oscillations could be separated for independent analysis. Each type of oscillation had a high and a low current state characterized by durations τ_{hi} and τ_{lo}, respectively. Probability distributions for τ_{hi} and τ_{lo} are shown for a sequence of fast RTS fluctuations in Figure 3.7 (A) and for slow RTS fluctuations in Figure 3.7 (B); the color scheme corresponds to the data in Figure 3.6 (B-D). All four distributions were well fit by single exponential time constants for periods of analysis shorter than $<\tau_{mem}>$. Analysis of much longer time periods resulted in biexponential distributions (Figure 3.7 (C, D)) and reflected the presence, in data sets extending over hundreds of seconds, of many sequences of both fast and slow RTS fluctuations. However, the fast and slow rates were sufficiently different that they appeared as two distinguishable slopes in Figure 3.7 (C, D). As a guide, blue and green colors have been applied to portions of the distribution that correspond to the fast and slow fluctuations, respectively.

Figure 3.7 (C, D) further provides a comparison of the probability distributions acquired at different pH values. The stability of the lysozyme devices allowed statistics to be accumulated for many minutes at each pH, all from the same attached enzyme. Figure 3.7 (C) shows that τ_{hi} was nearly independent over a pH range from 5 to 11; outside this pH range, lysozyme was no longer catalytically active[43-45]. Figure 3.7 (D), however, shows that τ_{lo} is much faster at pH 7 than at pH 5 or 11. The pH dependence of τ_{lo} in the long-duration, slow-switching region of the histogram, being much longer than the other three time constants, dominates the time-averaged properties of the lysozyme molecule.

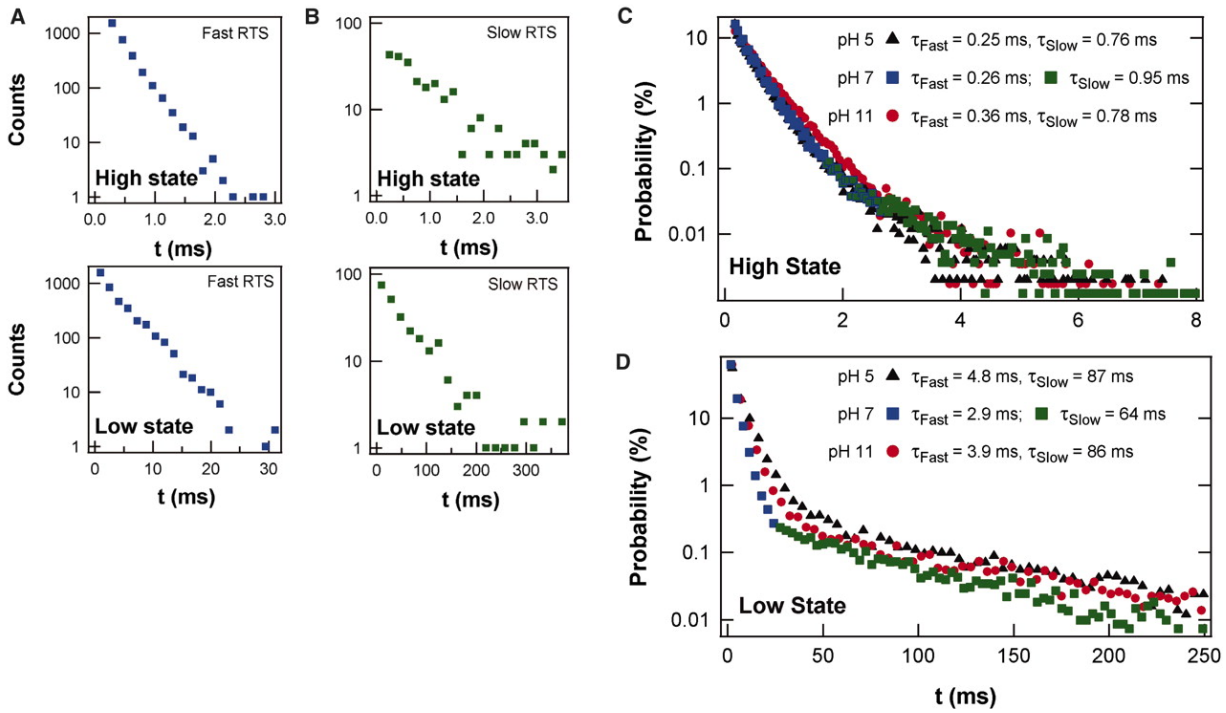

Figure 3.7: (A and B) Direct comparison of the probability distributions of the high state (τ_{hi}) and low state (τ_{lo}) durations during (A) fast and (B) slow RTS switching at pH 7. Both pairs of distributions derive from uninterrupted, 15-s data sets, though many fewer counts occur during the slower activity represented by (B). (C and D) Probability distributions of continuous, 300-s data sets include as many as 10^5 transitions extending over many conversions between fast and slow RTS fluctuations. The inclusion of both fast and slow RTS sequences produces distinct, double-exponential distributions. Color has been applied to portions of the distributions in (A) to (D) to highlight correspondences with Figure 3.6. Measurements at three different pH values show that the high-current state has almost no pH dependence (C). By contrast, the low-current state is at least 25% faster at pH 7 than at pH 5 or 11 (D). Reproduced from [34].

3.3.2 Extracting Turnover Rates and Energetics from RTS

Two important physical parameters could be calculated from the mean values of $<\tau_{lo}>$ and $<\tau_{hi}>$. Their sum represents one complete oscillation and defines a mean turnover rate, *k*, for the activity, where

$$k = \frac{1}{<\tau_{lo}> + <\tau_{hi}>} \tag{3.1}$$

The calculation of enzymatic reaction rates from single-molecule data has been reviewed by Xie[46]. The ratio of $<\tau_{lo}>$ and $<\tau_{hi}>$ also determines an energy separation, ΔE, between the two physical states responsible for the high and low I(t) values. Boltzmann statistics provides the relative thermodynamic probability of being in one state versus the other as

$$\Delta E = k_b T ln(\frac{<\tau_{hi}>}{<\tau_{lo}>}) \tag{3.2}$$

In total, we identified five independent parameters $<\tau_{hi}>$, $<\tau_{lo}>$, $<\tau_{mem}>$, *k*, and ΔE, all of which change when the lysozyme switches from its fast RTS state to its slow RTS state. Table 3.1 summarizes these parameters and their pH dependence for a single lysozyme molecule.

3.3.3. T4 Lysozyme Activity

Table 3.1 further lists the overall percentage of time spent in the fast or slow RTS states. This percentage is yet another independent parameter, being a nontrivial combination of the duration $<\tau_{mem}>$ and the regularity with which each behavior is observed. At pH 7, $<\tau_{mem}>$ was nearly equal for the fast and the slow RTS state, and the time in either state approached 50%. At non-neutral pH values, however, multiple changes skewed this balance. First, the number of inactive periods in which no switching was observed nearly doubled. This doubling, amplified by a modest increase in $<\tau_{mem}>$ of the inactive duration, resulted in a rapidly growing proportion of total inactive time. Moreover, we observed that inactive periods always interrupted sequences of fast RTS oscillations and doubled the number of fast RTS intervals observed while only modestly decreasing their duration $<\tau_{mem}>$. The increased time spent in inactive or fast RTS intervals both came at a cost to the percentage of time spent in the slow-switching RTS state, which was reduced to 19.7% at pH 11 and 15.7% at pH 5. This decrease occurred despite a substantial increase in $<\tau_{mem}>$, which considered in isolation would indicate an improving stability of the slow RTS state. We further note that the fast and slow RTS oscillation rates *k* both decreased by 25 to 35% away from pH 7; because they both decreased proportionally, the *k* values only minimally contributed to the pH dependence of the time spent in the fast or slow RTS states.

Table 3.1: Lysozyme activity rates. Reproduced from [34].

	Parameter	pH 5	pH 7	pH 11
Processing	$\langle\tau_{hi}\rangle$, ms	0.76 ± 0.05	0.95 ± 0.08	0.78 ± 0.09
(slow)	$\langle\tau_{lo}\rangle$, ms	87 ± 3.0	64 ± 2.0	86 ± 3.0
	ΔE, kcal/mol	2.84	2.53	2.82
	k, Hz	11.4	15.4	11.5
	$\langle\tau_{mem}\rangle$, s	9.3 ± 5.1	8.0 ± 3.0	12.0 ± 4.4
	% time in state	16.3%	41.1%	21.1%
	time-averaged catalytic rate, Hz	1.8	6.3	2.4
Nonproductive	$\langle\tau_{hi}\rangle$, ms	0.25 ± 0.01	0.26 ± 0.01	0.36 ± 0.01
(fast)	$\langle\tau_{lo}\rangle$, ms	4.80 ± 0.35	2.90 ± 0.10	3.90 ± 0.17
	ΔE, kcal/mol	1.77	1.45	1.43
	k, Hz	198	316	235
	$\langle\tau_{mem}\rangle$, s	6.2 ± 4.0	7.9 ± 2.3	5.4 ± 1.8
	% time in state	72.4%	52.1%	63.8%
Inactive	$\langle\tau_{mem}\rangle$, s	0.83 ± 0.63	0.72 ± 0.25	0.96 ± 0.53
	% time in state	11.3%	6.8%	15.0%

3.3.4. Randomness Parameter

Our long-duration data sets also enable analysis of the statistical variance of the τ_{lo} and τ_{hi} values. Any single-step Poisson process has a statistical variance $\sigma^2 = \langle t \rangle^2$. The normalized variance or randomness parameter

$$r \equiv \frac{\sigma^2}{\langle t \rangle^2} = \frac{\langle t^2 \rangle - \langle t \rangle^2}{\langle t \rangle^2} \tag{3.3}$$

is a powerful tool in single-molecule studies for distinguishing hidden intermediate steps along a reaction coordinate[47-49]. As shown in Table 3.2, analysis of individual τ_{lo} durations concludes that $r \approx 1$, indicating that the physical processes underlying the transition from I_{lo} to I_{hi} is in fact governed by a simple, single-step Poisson process. This conclusion remains true for both fast and slow RTS data at the different pH values tested, even though τ_{lo} differs by a factor of 20. By contrast, the physical process underlying the I_{hi} to I_{lo} transition has values of $r < 1$, indicating more complex processes. For example, n identical Poisson processes in succession will produce a distribution of durations τ that have a variance $r = 1/n$ [48,50]. Thus, lysozyme forms a closed conformation in a single step, but the transition back to its open configuration requires at least two steps. Although this finding is the same for both fast and slow RTS oscillations, the extra intermediate step required for opening is not necessarily the same in both cases. During processive sequences, the intermediate step could play a role in the catalysis and substrate turnover[51]. During fast sequences of nonproductive binding, it might be involved in

repositioning the substrate within the active site in an attempt to find a reactive bond for hydrolysis. Notably, the inactive state of lysozyme occurs when the enzyme closes around the substrate.

Table 3.2: Normalized variances of lysozyme rates. Reproduced from [34].

	Parameter	**pH 5**	**pH 7**	**pH 11**
Processing (slow)	r_{hi}	0.68 ± 0.15	0.74 ± 0.12	0.60 ± 0.15
	r_{lo}	1.00 ± 0.18	1.06 ± 0.15	1.11 ± 0.23
Nonproductive (fast)	r_{hi}	0.48 ± 0.10	0.43 ± 0.06	0.61 ± 0.08
	r_{lo}	0.97 ± 0.13	0.99 ± 0.09	1.00 ± 0.10

3.3.5 Static Disorder

The conductance signal of a single lysozyme device allowed us to directly determine multiple independent parameters, including seven independent time constants and their pH dependence, all without foreknowledge of the properties of either the enzyme or the SWNT. Out of 50 single-molecule devices, the presence of fast and slow RTS components was very reproducible, although there were variations in the numerical rates observed. For example, among seven lysozyme devices with high-quality signal-to-noise ratios, the rates of the slow RTS state at pH 7 varied from 10 to 50 Hz, with a mean $k = 24 \pm 15$ Hz. The rate of the fast RTS state varied from

127 to 461 Hz, with a mean k = 284 ± 127 Hz. Similar enzyme-to-enzyme variation has been observed previously using single molecule optical techniques[52-54], and has been attributed to static disorder, stationary heterogeneity arising from differences in the post-translational modification of identical amino acid sequences[53].

3.4 Comparison with Forster Resonance Energy Transfer

Next, we applied these empirical observations to examine the mechanism and catalytic activity of lysozyme, through detailed analysis of the electronic device signal from lysozyme-tethered nanocircuits. By comparing the I(t) signal to lysozyme dynamics known from ensemble and single-molecule Forster resonance energy transfer (FRET) experiments[55-58], we can draw several parallels (*e.g.*, lysozyme remains static in the absence of substrate). During substrate processing, lysozyme undergoes an 8 Å, hinge-like mechanical motion with two domains closing around the substrate[56,58-61]. FRET observations reveal that this motion occurs at two different rates: a slow hinge oscillation of 20 to 90 Hz corresponding to enzymatic turnover events, or else a more rapid, nonproductive movement at 200 to 400 Hz[45,56,58].

These FRET rates are in excellent agreement with our fast RTS and slow RTS oscillations, and the interconversion rate matches our $<\tau_{mem}>$ values. Thus, we conclude that the two-level electronic signal is caused by the lysozyme hinge motion, with slow RTS oscillations resulting from the transduction of catalytic turnover events and fast RTS oscillations corresponding to lysozyme's nonproductive binding events. These kinetic rates obtained with surface-bound lysozyme might differ from bulk rates, but FRET measurements with freely diffusing lysozyme

and surface-bound peptidoglycan[57] yield the same range of rates, suggesting that the consequences of tethering the lysozyme to a surface are minor.

The agreement demonstrates the equivalence of the lysozyme device data with FRET measurements, but in other ways the SWNT-lysozyme device data are more informative. Fluorophore bleaching and quenching limit the duration of FRET measurements on a single molecule and constrain the ability to observe slow conformational interconversions by FRET[45]. The I(t) measurement duration is not similarly limited, and the $<\tau_{mem}>$ values in Table 3.1 represent hundreds of such events by the same single molecule. Using such long time scales, we directly observed the same molecule changing from its productive conformation to its unproductive one. We also obtained the average percentage time spent in the slow RTS state, which when multiplied by *k* gave a time-averaged, effective catalytic rate for the single molecule. By collecting a true average over many conformational changes, this single-molecule rate approached the kinetics of an ensemble (Table 3.1). Furthermore, our I(t) records extend this single-molecule insight to different pH conditions.

3. 5 Summary of Device Parameters of Protein-Conjugated SWNTs

Of 20 SWNT devices conjugated with lysozyme and tested for activity, 18 showed the combination of fast RTS and slow RTS states described in the main text. Table 3.3 below summarizes important device parameters for five devices made from semiconductors (s-SWNTs) and five more made from metals (m-SWNTs). Here, we describe some of the noteworthy similarities and trends observed.

As-fabricated devices have a wide range of contact resistances and, subsequently, initial device resistances $R_{pristine}$. Table 3.3 includes a few examples of the minimum achievable contact resistance, which for our diameter SWNT is approximately 0.1 – 0.3 MΩ . We also tabulate the increase in DC resistance $\Delta R_{coating}$ that occurs after pyrene coating and protein conjugation. For the low resistance devices, functionalization adds 0.8 – 2.7 MΩ to the device resistance (at V_G = 0). Low resistance m-SWNTs and s-SWNTs both show the same range of changes, which indicates that simple electrostatic shifts of the $I(V_G)$ characteristics cannot be the primary mechanism responsible for the increase. Instead, we interpret $\Delta R_{coating}$ to be extra scattering along the SWNT sidewall caused by the attached molecules. Devices #4, 5, and 10 begin with anomalously high $R_{pristine}$ values and consequently increase resistance much more dramatically upon functionalization.

All of the devices in Table 3.3, as well as the control devices described above, do exhibit changes ΔI in their DC currents when the local environment is changed. In other words, the step in Figure 3.1 (D) at t = 0 is by no means unique, and similar results have been reported for a wide range of different analytes, using either pristine or functionalized SWNTs. Reviews of this phenomenon have been published recently[42,62]. What distinguishes the control devices from those in Table 3.3, however, is the presence of two level fluctuations. No such fluctuations are observed in the control devices.

Table 3.3 tabulates mean values of the different current levels observed for each device. In particular, the current measured in PBS (I_{PBS}) can be compared to the high (I_{hi}) and low (I_{lo})

current values observed when the same device is switching. The general trend is for I_{lo} to be quite similar to I_{PBS}, which suggests that I_{lo} corresponds to the unbound configuration of lysozyme. I_{hi}, on the other hand, is substantially larger and is assigned to the bound substrate-lysozyme complex. We note that the inactive state described above is inactive at the I_{lo} current level, proving that the inactive state is also an unbound configuration. While this assignment is likely to be correct, the trend is not without apparent exceptions. Four of the m-SWNT devices have $I_{lo} \approx I_{PBS}$, but in device #9 both currents I_{hi} and I_{lo} are substantially higher than would be expected from R_{coated}. Continuous measurements prove that R_{coated} is a very poor benchmark, because its value varies in time and is dependent on surface charge transfer and the liquid electrolyte potential, strongly so for s-SWNT devices.

The most reliable parameter, we believe, is the relative difference $\Delta I_{RTS} = (I_{hi} - I_{lo}) / I_{lo}$, because ΔI_{RTS} is insensitive to slowly varying processes. Background removal techniques shown in Figure 3.6 (A, B) are very effective for the statistical analysis of ΔI_{RTS}. This reliability leads to the very uniform values of ΔV_G which will be discussed in detail in Chapter 4. DC changes in current are, by comparison, extremely difficult to attribute to any particular source. This reliability issue underscores a main difficulty in using nanoscale devices as DC chemical or biological sensors, and their promise for monitoring dynamic processes as reported here.

Because of this high degree of reliability, it is particularly noteworthy that ΔI has the same distribution of values for both fast RTS and slow RTS oscillations, and it suggests the enzyme undergoes a similar range of conformational motions during both types of oscillation. Indeed,

FRET proves that a lysozyme's range of mechanical motion is the same for both types of activity[45,57,58].

Table 3.3: SWNT-Lysozyme device characteristics. Reproduced from [34]

#	Type	$R_{pristine}$ (MΩ)	R_{coated} (MΩ)	$\Delta R_{coating}$ (MΩ)	I_{PBS} (nA)	I_{lo} (nA)	I_{hi} (nA)	ΔI_{RTS} (%)	dI/dV_g (%/V)	ΔV_G (V) calc
1	s-SWNT	0.28	1.2	0.9	36*	40*	48*	+20%	95	0.21
2	s-SWNT	0.38	1.5	1.1	87	103	122	+18%	88	0.21
3	s-SWNT	0.34	3.0	2.7	5.65	7	10.5	+50%	266	0.19
4	s-SWNT	17.6	56	38	2.5	2.8	2.9	+4%	20	0.20
5	s-SWNT	26.1	40	14	7.0	7.2	8.2	+14%	70	0.20
6	m-SWNT	0.10	1.4	1.3	78	80	82	+3%	18	0.16
7	m-SWNT	0.30	2.0	1.7	54	54	58	+7%	46	0.15
8	m-SWNT	0.35	2.6	2.2	42	45	50	+10%	54	0.19
9	m-SWNT	1.0	1.8	0.8	55	80	83	+4%	21	0.18
10	m-SWNT	3.0	30	27.1	3.5	3.3	4.9	+47%	235	0.20

*Measured at V_{sd} = 50 mV.

3.6 Lysozyme Processivity

As visualized by FRET on bacterial surfaces, lysozyme adheres to the peptidoglycan for long periods of time[57]. Such observations suggest, but do not prove, that lysozyme processively catalyzes the hydrolysis of a large number of glycosidic bonds before dissociation. FRET also proves that lysozyme interrupts its catalytic glycosidic hydrolysis with periods of rapid

movements that do not result in bond hydrolysis[45]. However, the degree of processivity, the reason for the rapid nonproductive motions, and the effects of substrate cross-linking remain incompletely understood for two main reasons. First, the peptidoglycan is highly heterogeneous in size and features a heavily cross-linked structure involving connections of the NAM subunits of the polysaccharide chains by pentapeptides[41,57]. Second, FRET and other optical techniques are limited by fluorophore bleaching, which prevents long-term measurement of the same individual molecule. Such considerations motivate the development of new methods for examining single proteins.

To address these issues, two developments are reported here. First, we synthesized a linear peptidoglycan substrate for lysozyme that includes non-cross-linked tripeptides (Figure 3.8). Second, we developed nanocircuits comprising individual lysozyme molecules attached to single-walled carbon nanotube (SWNT) field-effect transistors (FETs). The dynamic motions of the attached lysozyme induce fluctuations in the SWNT-FET conductance through a charge gating effect, similar to previous work with SWNT-FET sensors[16,39,63]. This electronic rather than optical transduction allows monitoring of the dynamic interactions of individual lysozyme molecules over long periods of time. Combining these two advances has provided new insights into lysozyme processing of peptidoglycans.

Devices were exposed to excess substrate and measured for 600 s; the same device was then thoroughly rinsed with water to remove surface-bound substrate before being probed a second time with a different substrate. The two substrates were tested in alternating orders on different devices to protect against systematic bias. Our analysis filtered the DC and lowest frequency

(<10 Hz) AC components of G(t) in order to focus on time-varying fluctuations and transients of ΔG(t).

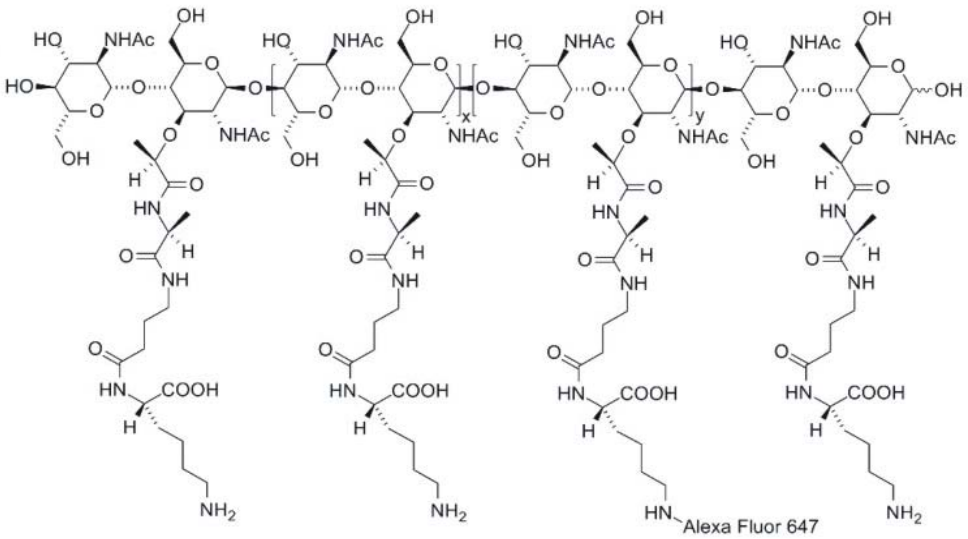

Figure 3.8: Chemical structure of the synthesized peptidoglycan substrate. Reproduced from [35].

Three distinct behaviors were observed and are categorized in Figure 3.9. The most common behavior was two-state G(t) fluctuation switching asymmetrically at an average rate of 30.0 Hz (Figure 3.9 (A), colored green). A second behavior involved fluctuations between the same two G(t) levels at the much higher average rate of 287 Hz (Figure 3.9 (B), blue). A relatively featureless, inactive behavior also occurred (Figure 3.9 (C), black), though this was primarily observed when measurements were performed in the absence of the lysozyme substrate peptidoglycan. Previous FRET measurements have proven that lysozyme motions are absent or disorganized in the absence of substrate but that, when present, substrate can drive one-dimensional hinge bending motions at the same two rates we observed[45]. The lower rate is

understood to be caused by productive processing of substrate by the enzyme, while the higher rate is associated with nonproductive, catalytically ineffective motions of the lysozyme[45].

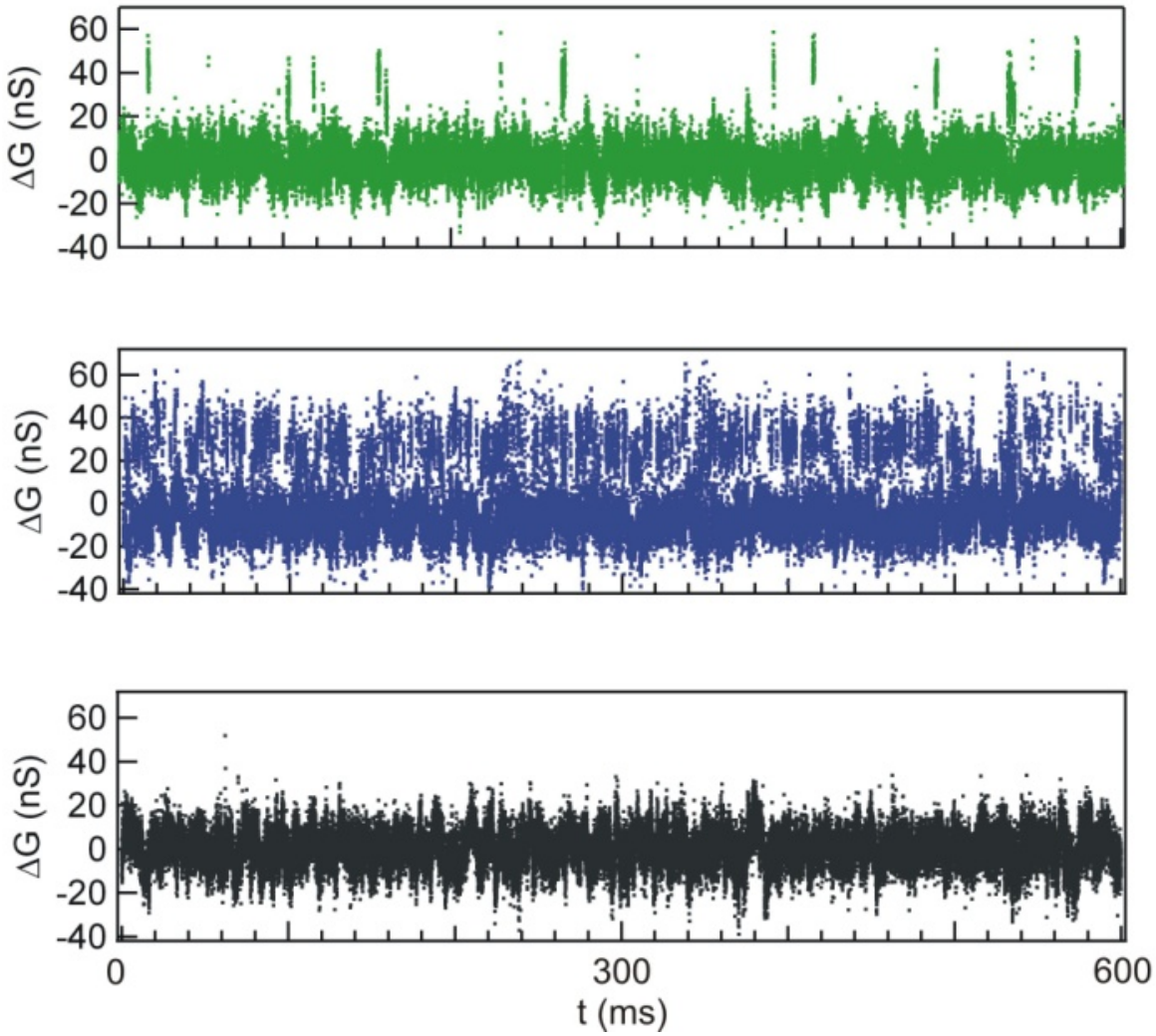

Figure 3.9: Source–drain conductance fluctuations ΔG(t) of a lysozyme device in the presence of the cross-linked substrate. The colors differentiate the three types of observed signal behavior, which included (A) slow switching with catalytic turnover (green), (B) rapid nonproductive switching (blue), and (C) inactivity (black). Reproduced from [35].

Long-duration measurements on single lysozyme molecules are possible with the SWNT-FET architecture. Five example measurements are shown in Figure 3.10 with the data points colored

to correspond to the three behaviors defined above. Figure 3.10 (A-C) was obtained from a single lysozyme device measured either without substrate (Figure 3.10 (A)) or with one of two different substrates described in more detail below.

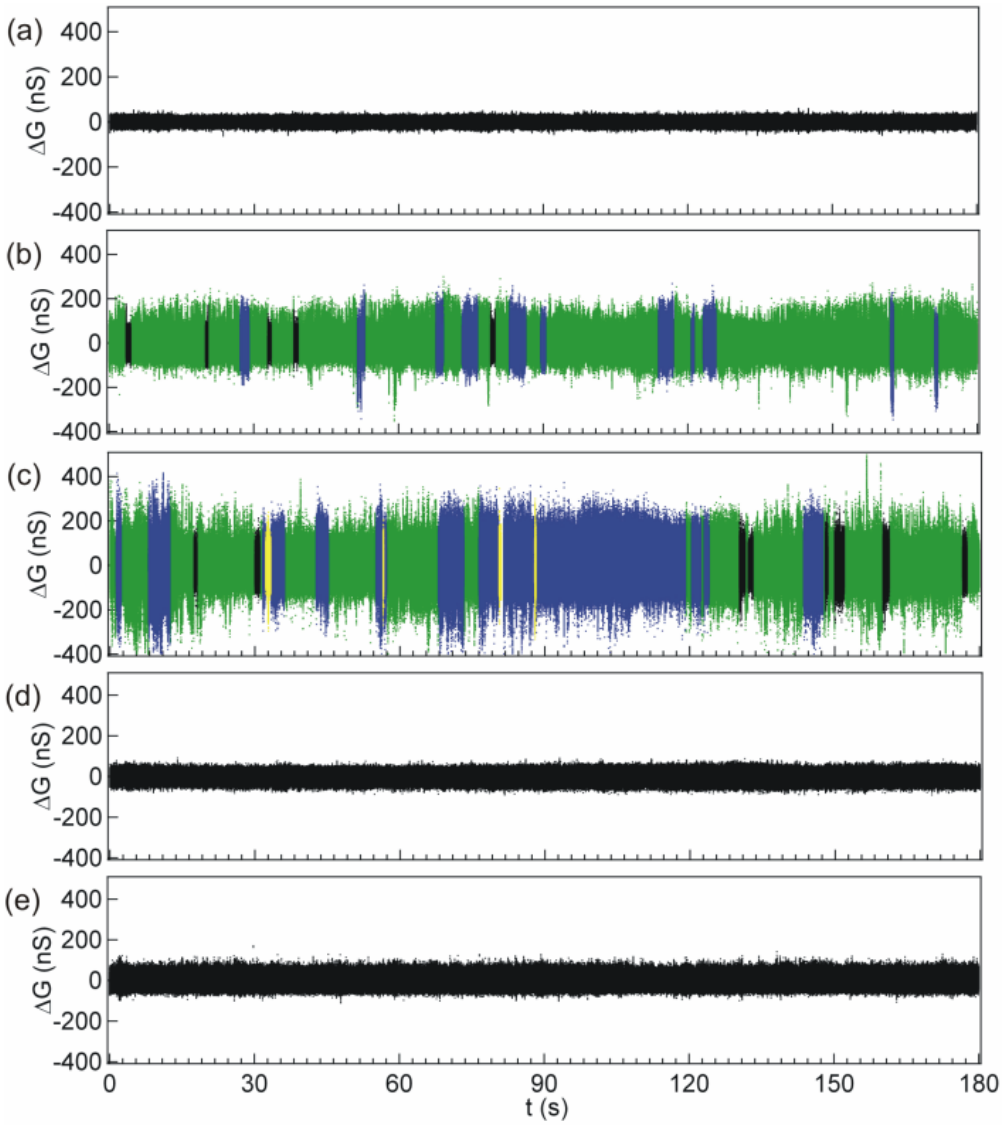

Figure 3.10: Long-duration source–drain conductance fluctuations. (A) In the absence of substrate, no conductance fluctuations were observed, as demonstrated here for a single lysozyme device incubated in phosphate buffer. Addition of the (B) linear or (C) cross-linked substrate resulted in the switching described in the text. Control experiments using the (D) E11H or (E) T26E catalytically inactive T4 lysozyme variant showed no activity when probed with the cross-linked (shown) or linear (not shown) substrate. Reproduced from [35].

The main focus of this section is to compare lysozyme processing of two different peptidoglycan substrates, one linear and the other cross-linked. Designed to mimic bacterial cell walls, the linear substrate featured an extended $(NAG\text{-}NAM)_n$ polysaccharide. Appended to each NAM subunit were tripeptides that were linked to lactic acid but did not cross-link polysaccharide fragments (Figure 3.8). Alexa Fluor 647 dye was incorporated at a density of ~5% on the peptides; the fluorophore was not used in the present experiments and would not be expected to alter the enzyme dynamics. Commercially obtained cell walls of peptidoglycan from *Micrococcus luteus* provided a second substrate for an examination of the effects of substrate cross-linking on the enzyme catalysis.

Figure 3.10 (B, C) shows a comparison of the catalytic activities of lysozyme processing of linear and cross-linked substrates, respectively. Both substrates allowed processive catalysis by lysozyme (green segments) but exhibited different proportions of the nonproductive (blue) and inactive (black) behaviors. T4 lysozyme does not require, nor is it hindered by, the peptide cross-links of the substrate for its processive movement. Nevertheless, the linear substrate fundamentally altered the distribution of the lysozyme dynamics. Figure 3.11 summarizes the analysis of 24 independent measurements performed using 14 different devices, of which Figure 3.10 is representative. On average, lysozyme spent 88% of the total time processing the linear substrate and made few rapid, nonproductive motions (7% of its time).

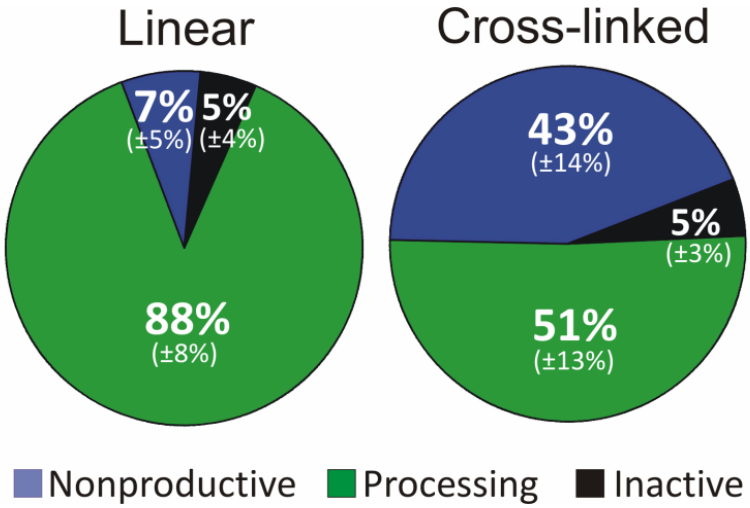

Figure 3.11: Percentages of lysozyme activities in the presence of the (left) linear or (right) cross-linked peptidoglycan substrate. The standard deviations for the activities are indicated in parentheses (n = 6 for the linear substrate and n = 8 for the cross-linked substrate). Reproduced from [35].

This processing of linear substrate contrasts sharply with observations made in the presence of the cross-linked substrate. The lysozyme increased the amount of time spent in rapid, nonproductive motions from 7 to 43% in the presence of the cross-linked peptidoglycan substrate (Figure 3.11). This difference in activity was very reproducible, regardless of whether the cross-linked or linear substrate was tested first. Furthermore, no degradation of lysozyme activity was observed during the reported experiments.

Another method for comparing the two lysozyme substrates is to analyze a power spectral density (PSD) plot of the raw data. Figure 3.12 compares PSD plots of the cross-linked (blue) and linear (green) substrates. The analysis reveals a substantial decrease in motion centered around 300 Hz. Such nonproductive binding events can thus be ascribed to differences in the substrates, not the enzyme.

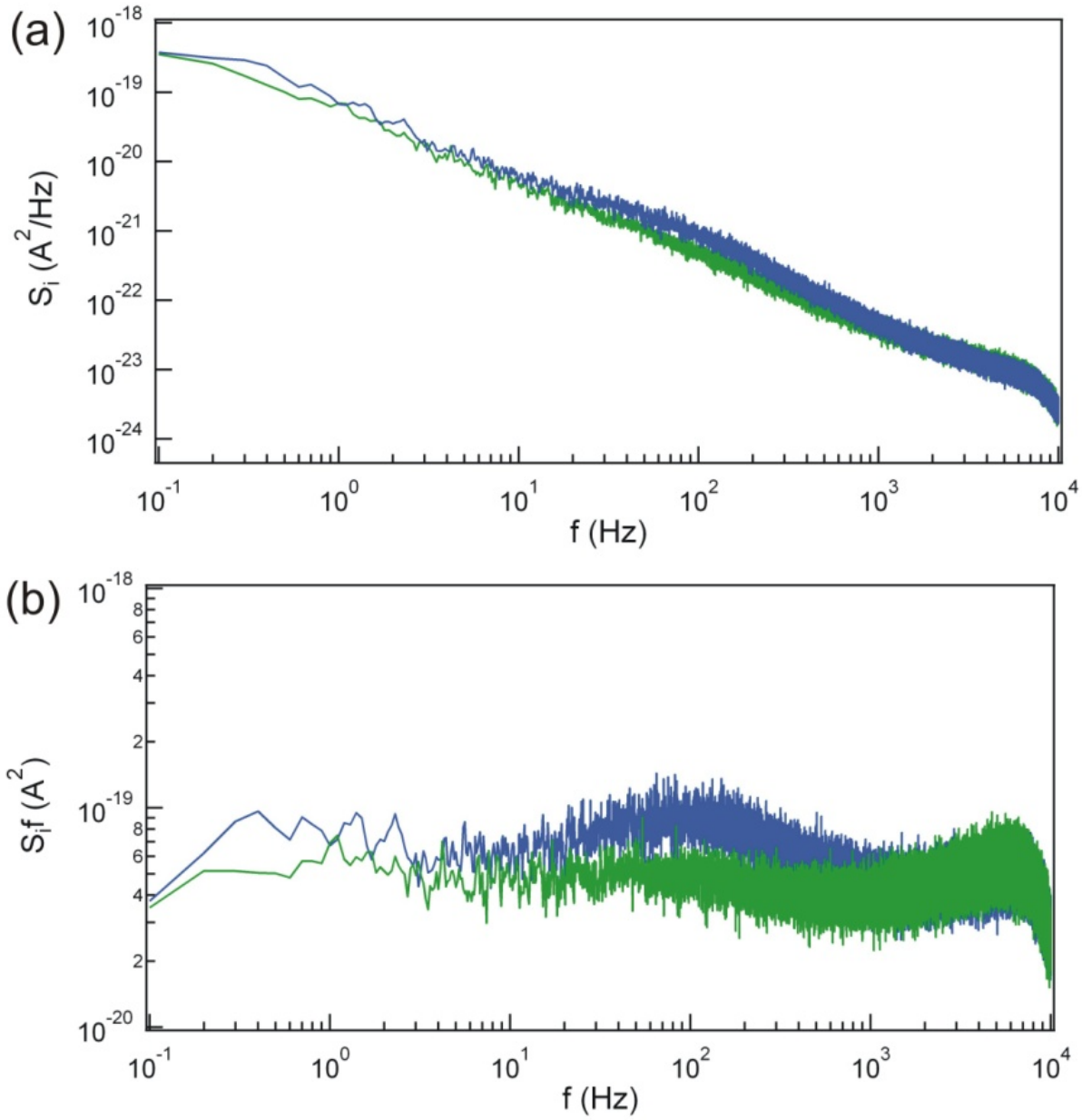

Figure 3.12: (A) PSD and (B) normalized PSD of (A) analysis comparing lysozyme activity in the presence of the cross-linked (blue) and linear (green) peptidoglycan. Reproduced from [35].

Monitoring of serial processing the two different types of substrates by the same lysozyme molecule proved that the peptide cross-links trap the enzyme in this rapidly oscillating, nonproductive state. We hypothesize that lysozyme catalysis stalls before attempting to transit a

cross-link to reach a neighboring polysaccharide. Thus, lysozyme could zigzag across the cell wall as it processively catalyzes glycoside hydrolysis and passes across peptide cross-links.

Despite the major differences in the distribution of enzyme activities, the two substrates had chemically identical glycosidic bonds and resulted in remarkably similar kinetic rates. The fluctuation in the rates of catalytic processing (Figure 3.9 (A)) and nonproductive motion (Figure 3.9 (B)) changed only slightly, if at all, when one substrate was substituted for another. Ambiguity in this comparison was caused by the static disorder of individual enzymes and the local environment of the enzyme tethered to the SWNT-FETs, both of which contributed to broad rate distributions. For example, the instantaneous single-molecule rates of catalytic turnover with the cross-linked substrate ranged from 17 to 59 Hz. Nevertheless, quantitative comparisons were made by averaging the mean rates (reported here with one standard deviation) from 100 s segments across multiple devices. Accordingly, the rate of catalytic turnover decreased 16%, from 35.9 ± 17.6 Hz (n = 9) for the linear substrate to 30.0 ± 14.5 Hz (n = 15) for the cross-linked substrate. The rate of nonproductive motions decreased 13%, from 329 ± 167 Hz for the linear substrate to 287 ± 184 Hz for the cross-linked substrate. Although the two substrates had overlapping ranges, the cross-linked substrate did appear to result in slightly lower rates. As might be expected, the presence of cross-links appears to slow the catalytic processing. The additional slowing of the nonproductive motions is consistent with a model in which the enzyme transits from one polysaccharide to another at cross-linked points.

The linear and cross-linked peptidoglycans exhibited similar percentages of inactive time (black data in Figures 3.8 and 3.9). During these inactive periods, which had an average duration of

1.06 s, no switching by the lysozyme device was observed, and G(t) remained in its low state. This low G(t) state was identical to the value observed when no substrate was present (Figure 3.13 (B, D)). Furthermore, the inactive periods occurred exclusively during periods of catalytic processing (green) and were never observed during the putative enzyme transits at peptide cross-links (blue). These observations suggest that the inactive period is caused by dissociation that occurs when lysozyme processes to the end of a polysaccharide substrate. In this interpretation, lysozyme proceeds along the polysaccharide backbone, catalyzing the hydrolysis of multiple glycosidic bonds before dissociation occurs. Upon association of new substrate, the inactive period concludes. We observed that the enzyme always returned to a substrate-processing state (green).

Finally, we note a fourth type of behavior that was observed only with the cross-linked substrate and is represented by the yellow color in Figure 3.10 (C). These segments correspond to novel behavior in which rapid, nonproductive motion at the peptide cross-links is interrupted for 0.5–3.0 s with G(t) stuck at its high value. Whereas the inactive periods discussed above are associated with dissociation events because of their low G(t), these pauses at high G(t) imply that the enzyme is stuck in an enzyme-closed, substrate-bound configuration (Figure 3.13 (C, E)). This state occurs randomly and with a low probability, and it appears to be independent of the return to catalytic processing.

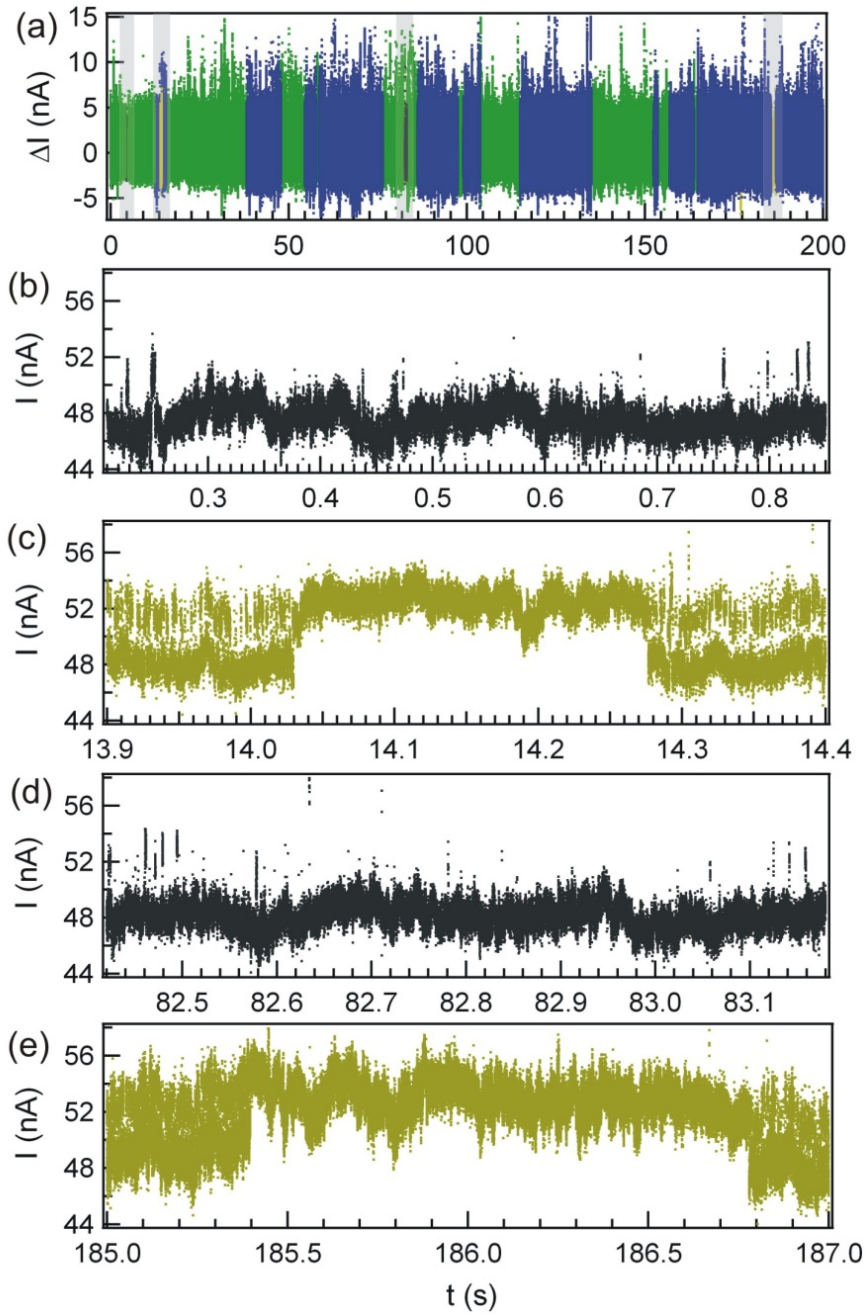

Figure 3.13: Conductance fluctuations of a single lysozyme nanocircuit in the presence of crosslinked substrate. The color differentiates lysozyme activity, which include slow catalytic processing (green), rapid nonproductive motions (blue), and inactivity (black or yellow). One type of inactivity (black) consists of unusually long durations in the low current state, interrupting sequences of slow two-level switching (B, D). The second type of inactivity (yellow) consists of long durations in the high current state, interrupting sequences of fast two-level switching (C, E). The latter type of inactivity occurs with cross-linked substrate but not linear substrate. Reproduced from [35].

3.7 Summary

The results presented here demonstrate the tremendous potential of molecular electronics to uncover fundamental knowledge in biophysics. Lysozyme orthologues have been studied for over a century, yet the nanocircuits reported here have unveiled new information about T4 lysozyme's activities and dynamics, including its processivity and potential ability to transit peptide cross-links. Lysozyme proceeds linearly to the ends of the linear substrate but could sidestep over peptide cross-links of the cross-linked substrate. This study providing a relationship between lysozyme dynamics and function will allow deeper understanding of the precise lysozyme motions for digesting the bacterial cell wall and could guide the design of new enzymes for antibacterial and other applications.

Furthermore, this nanocircuit architecture is complementary to more traditional fluorescence techniques, but with the advantages that fluorescent labels are not required, the transduction mechanism does not bleach, and electronic bandwidths extend temporal resolution into the single-microsecond regime. These advantages provide a framework for exploring dynamics of other enzymes.

Bibliography

[1] J. Kong, N. R. Franklin, C. W. Zhou, M. G. Chapline, S. Peng, K. J. Cho, and H. J. Dai, Science **287**, 622 (2000).

[2] P. G. Collins, K. Bradley, M. Ishigami, and A. Zettl, Science **287**, 1801 (2000).

[3] J. Kong, A. Javey, K.-J. Lee, and J. Kong, in *Carbon Nanotube Electronics* (Springer US, 2009), pp. 191.

[4] I. Heller, A. M. Janssens, J. Männik, E. D. Minot, S. G. Lemay, and C. Dekker, Nano Letters **8**, 591 (2008).

[5] K. Bradley, J.-C. P. Gabriel, A. Star, and G. GrÃ¼ner, Applied Physics Letters **83**, 3821 (2003).

[6] J. Zhang, A. Boyd, A. Tselev, M. Paranjape, and P. Barbara, Applied Physics Letters **88** (2006).

[7] J. L. Bahr, J. Yang, D. V. Kosynkin, M. J. Bronikowski, R. E. Smalley, and J. M. Tour, Journal of the American Chemical Society **123**, 6536 (2001).

[8] B. R. Goldsmith, J. G. Coroneus, A. A. Kane, G. A. Weiss, and P. G. Collins, Nano Letters **8**, 189 (2008).

[9] B. R. Goldsmith, J. G. Coroneus, V. R. Khalap, A. A. Kane, G. A. Weiss, and P. G. Collins, Science **315**, 77 (2007).

[10] M.-L. Sham and J.-K. Kim, Carbon **44**, 768 (2006).

[11] R. J. Chen, Y. G. Zhan, D. W. Wang, and H. J. Dai, J. Am. Chem. Soc. **123**, 3838 (2001).

[12] S. A. Claridge, J. J. Schwartz, and P. S. Weiss, ACS Nano **5**, 693 (2011).

[13] W. Min, B. P. English, G. B. Luo, B. J. Cherayil, S. C. Kou, and X. S. Xie, Accounts of Chemical Research **38**, 923 (2005).

[14] R. Roy, S. Hohng, and T. Ha, Nat. Methods **5**, 507 (2008).

[15] A. Star, J. C. P. Gabriel, K. Bradley, and G. Grüner, Nano Letters **3**, 459 (2003).

[16] K. Besteman, J. O. Lee, F. G. M. Wiertz, H. A. Heering, and C. Dekker, Nano Letters **3**, 727 (2003).

[17] A. Star, V. Joshi, T. R. Han, M. V. P. Altoe, G. Grüner, and J. F. Stoddart, Organic Letters **6**, 2089 (2004).

[18] G. Grüner, Analytical and Bioanalytical Chemistry **384**, 322 (2006).

[19] Y. Cui, Q. Q. Wei, H. K. Park, and C. M. Lieber, Science **293**, 1289 (2001).

[20] F. Patolsky, G. Zheng, O. Hayden, M. Lakadamyali, X. Zhuang, and C. M. Lieber, Proc. Natl. Acad. Sci. U. S. A. **101**, 14017 (2004).

[21] F. Patolsky, G. F. Zheng, and C. M. Lieber, Analytical Chemistry **78**, 4260 (2006).

[22] F. Patolsky, B. P. Timko, G. H. Yu, Y. Fang, A. B. Greytak, G. F. Zheng, and C. M. Lieber, Science **313**, 1100 (2006).

[23] S. J. Park, T. A. Taton, and C. A. Mirkin, Science **295**, 1503 (2002).

[24] Y. Xiao, F. Patolsky, E. Katz, J. F. Hainfeld, and I. Willner, Science **299**, 1877 (2003).

[25] F. Schedin, A. K. Geim, S. V. Morozov, E. W. Hill, P. Blake, M. I. Katsnelson, and K. S. Novoselov, Nat Mater **6**, 652 (2007).

[26] S. Huang *et al.*, Nat Nano **5**, 868 (2010).

[27] M. Tsutsui, S. Rahong, Y. Iizumi, T. Okazaki, M. Taniguchi, and T. Kawai, Sci. Rep. **1** (2011).

[28] S. Sorgenfrei, C.-y. Chiu, R. L. Gonzalez, Y.-J. Yu, P. Kim, C. Nuckolls, and K. L. Shepard, Nat Nano **6**, 126 (2011).

[29] S. Sorgenfrei, C.-y. Chiu, M. Johnston, C. Nuckolls, and K. L. Shepard, Nano Letters **11**, 3739 (2011).

[30] A. Müller, S. K. Das, P. Kogerler, H. Bögge, M. Schmidtmann, A. X. Trautwein, V. Schünemann, E. Krickemeyer, and W. Preetz, Angew. Chem.-Int. Edit. **39**, 3414 (2000).

[31] A. Müller, S. K. Das, H. Bögge, M. Schmidtmann, A. Botar, and A. Patrut, Chem. Commun., 657 (2001).

[32] L. An, J. M. Owens, L. E. McNeil, and J. Liu, Journal of the American Chemical Society **124**, 13688 (2002).

[33] G. T. Hermanson, *Bioconjugate Techniques* (Academic Press, Inc., Chicago, 2008), 2nd edn.

[34] Y. Choi, I. S. Moody, P. C. Sims, S. R. Hunt, B. L. Corso, I. Perez, G. A. Weiss, and P. G. Collins, Science **335**, 319 (2012).

[35] Y. Choi, I. S. Moody, P. C. Sims, S. R. Hunt, B. L. Corso, D. E. Seitz, L. C. Blaszczak, P. G. Collins, and G. A. Weiss, Journal of the American Chemical Society **134**, 2032 (2012).

[36] Y. Choi, T. J. Olsen, P. C. Sims, I. S. Moody, B. L. Corso, M. N. Dang, G. A. Weiss, and P. G. Collins, Nano Letters **13**, 625 (2013).

[37] R. Kuroki, L. H. Weaver, and B. W. Matthews, Proceedings of the National Academy of Sciences of the United States of America **96**, 8949 (1999).

[38] S. Rosenblatt, Y. Yaish, J. Park, J. Gore, V. Sazonova, and P. L. McEuen, Nano Letters **2**, 869 (2002).

[39] R. J. Chen, S. Bangsaruntip, K. A. Drouvalakis, N. W. S. Kam, M. Shim, Y. M. Li, W. Kim, P. J. Utz, and H. J. Dai, Proceedings of the National Academy of Sciences of the United States of America **100**, 4984 (2003).

[40] R. J. Chen, H. C. Choi, S. Bangsaruntip, E. Yenilmez, X. Tang, Q. Wang, Y.-L. Chang, and H. Dai, Journal of the American Chemical Society **126**, 1563 (2004).

[41] S. O. Meroueh, K. Z. Bencze, D. Hesek, M. Lee, J. F. Fisher, T. L. Stemmler, and S. Mobashery, Proceedings of the National Academy of Sciences of the United States of America **103**, 4404 (2006).

[42] T. Zhang, S. Mubeen, N. V. Myung, and M. A. Deshusses, Nanotechnology **19** (2008).

[43] A. Tsugita, M. Inouye, E. Terzaghi, and Streisin.G, J. Biol. Chem. **243**, 391 (1968).

[44] H. B. Jensen and K. Kleppe, European Journal of Biochemistry **28**, 116 (1972).

[45] Y. Chen, D. H. Hu, E. R. Vorpagel, and H. P. Lu, J. Phys. Chem. B **107**, 7947 (2003).

[46] S. N. Xie, Single Molecules **2**, 229 (2001).

[47] K. Svoboda, P. P. Mitra, and S. M. Block, Proceedings of the National Academy of Sciences of the United States of America **91**, 11782 (1994).

[48] M. J. Schnitzer and S. M. Block, Cold Spring Harbor Symposia on Quantitative Biology **60**, 793 (1995).

[49] W. L. Xu, J. S. Kong, and P. Chen, Journal of Physical Chemistry C **113**, 2393 (2009).

[50] M. J. Schnitzer and S. M. Block, Nature **388**, 386 (1997).

[51] G. Bhabha, J. Lee, D. C. Ekiert, J. Gam, I. A. Wilson, H. J. Dyson, S. J. Benkovic, and P. E. Wright, Science **332**, 234 (2011).

[52] Q. Xue and E. S. Yeung, Nature **373**, 681 (1995).

[53] D. B. Craig, E. A. Arriaga, J. C. Y. Wong, H. Lu, and N. J. Dovichi, Journal of the American Chemical Society **118**, 5245 (1996).

[54] X. S. Xie and H. P. Lu, J. Biol. Chem. **274**, 15967 (1999).

[55] H. P. Lu, L. Y. Xun, and X. S. Xie, Science **282**, 1877 (1998).

[56] H. P. Lu, Curr. Pharm. Biotechnol. **5**, 261 (2004).

[57] D. H. Hu and H. P. Lu, Biophysical Journal **87**, 656 (2004).

[58] Y. Wang and H. P. Lu, J. Phys. Chem. B **114**, 6669 (2010).

[59] H. R. Faber and B. W. Matthews, Nature **348**, 263 (1990).

[60] G. E. Arnold, J. I. Manchester, B. D. Townsend, and R. L. Ornstein, Journal of Biomolecular Structure & Dynamics **12**, 457 (1994).

[61] B. L. de Groot, S. Hayward, D. M. F. van Aalten, A. Amadei, and H. J. C. Berendsen, Proteins-Structure Function and Genetics **31**, 116 (1998).

[62] X. Y. Sun and Y. G. Sun, Journal of Materials Science & Technology **24**, 569 (2008).

[63] C. Li, M. Curreli, H. Lin, B. Lei, F. N. Ishikawa, R. Datar, R. J. Cote, M. E. Thompson, and C. Zhou, Journal of the American Chemical Society **127**, 12484 (2005).